Journal of Materials Research and Technology 27 (2023) 6961–6973

Contents lists available at ScienceDirect

Journal of Materials Research and Technology

journal homepage: www.elsevier.com/locate/jmrt

Laser printed amorphous magnesium alloy: Microstructure, mechanical properties and degradation behavior

Cheng Chen [a,1], Shaoyu Li [a,1], Chenrong Ling [a], Youwen Yang [a,b,*], Chengde Gao [c], Yageng Li [d], Xinyi Xiao [e], Wenhao Zhou [f], Cijun Shuai [a,c,**]

[a] Institute of Additive Manufacturing, Jiangxi University of Science and Technology, Nanchang, 330013, PR China
[b] Key Laboratory of Construction Hydraulic Robots of Anhui Higher Education Institutes, Tongling University, Tongling, 244061, PR China
[c] State Key Laboratory of High Performance Complex Manufacturing, Central South University, Changsha, 410083, PR China
[d] Beijing Advanced Innovation Center for Materials Genome Engineering, University of Science and Technology Beijing, Beijing, 100083, PR China
[e] Mechanical Engineering Department, University of North Texas, Denton, TX, USA
[f] Shaanxi Key Laboratory of Biomedical Metallic Materials, Northwest Institute for Non-Ferrous Metal Research, Xi'an, PR China

ARTICLE INFO

Handling editor: Carlos Ruestes

Keywords:
Amorphous magnesium alloy
Laser powder bed fusing
Corrosion behavior
Mechanical properties
Biocompatibility

ABSTRACT

Amorphous magnesium (Mg) alloy, especially Mg–Zn–Ca series, has been receiving continuous attention in biomedical field, because of its favorable corrosion resistance, suitable modulus and biocompatibility. In this work, laser powder bed fusing (LPBF) with unique characteristics of rapid solidification and layer-by-layer fashion was used to fabricate bulk Mg–Zn–Ca and Mg–Zn–Ca–Y amorphous parts. It was revealed that the as-built parts contained amorphous structure, since the molten pool experienced an extremely high cooling rate that suppressed ordered arrangement of atoms. A few of nanocrystals (α-Mg and $Ca_2Mg_5Zn_{13}$) were obtained due to repeated heat accumulation in heat-affected zones. More significantly, Y alloying altered the glass forming ability and stimulated in-situ formation of quasicrystal I-phase with high hardness and elastic modulus, which not only acted as reinforced particles, but also retarded the propagation of shear bond and thereby excited the emergence of secondary shear bands and vein patterns. Thus, Mg–Zn–Ca–Y part exhibited simultaneously improved yield strength and plasticity. Despite the micro galvanic corrosion induced by crystalline phases, it exhibited a moderate corrosion rate. Furthermore, in vitro cell tests proved its favorable biocompatibility. Our work highlighted the feasibility to prepare amorphous Mg alloy with controllable performance.

1. Introduction

Magnesium (Mg) alloy is regarded as a new generation revolutionary medical metal because of its distinctive biodegradability, appropriate mechanical properties, excellent osseointegration performance and biocompatibility [1–4]. The Mg ions generated from degradation can be absorbed through metabolism, and even promote osteoblasts [5,6]. In addition, its young's modulus (~45 GPa) is close to that of natural bone tissue (15–30 GPa), effectively mitigating the stress shielding effect [7,8]. However, Mg alloy degrades too rapid in vivo that contains highly corrosive chloride ions and other organic molecules, resulting in premature collapse of structural integrity and rapid decay of mechanical properties. Consequently, current Mg-based devices like bone scaffold or cardiovascular stent are hardly to fulfill the desirable service life (generally 6–12 months) [9,10]. Up to now, several strategies, such as purification, alloying treatment and surface coating, have been proposed to improve the corrosion resistance of Mg alloy, and are achieving substantial progress [11–13].

Amorphization is another practicable measure to enhance the corrosion resistance of Mg alloy. Amorphous alloy, known as metallic glass, owns homogeneous microstructure with short-range ordered and long-range disordered atomic arrangement. They are free of crystal structure defects such as grain boundaries and dislocations, and thus exhibit better anti-corrosion ability than corresponding polycrystalline alloy [14,15]. Gu et al. [16] revealed that amorphous Mg–Zn–Ca alloy alleviated galvanic corrosion and localized corrosion. During

* Corresponding author. Jiangxi University of Science and Technology, Ganzhou, 341000, PR China.
** Corresponding author. Cijun Shuai Jiangxi University of Science and Technology, Ganzhou, 341000, PR China.
E-mail addresses: yangyouwen@jxust.edu.cn (Y. Yang), shuai@csu.edu.cn, shuai@jxust.edu.cn (C. Shuai).
[1] These authors contributed equally to this work.

https://doi.org/10.1016/j.jmrt.2023.11.095
Received 23 September 2023; Received in revised form 23 October 2023; Accepted 11 November 2023
Available online 17 November 2023

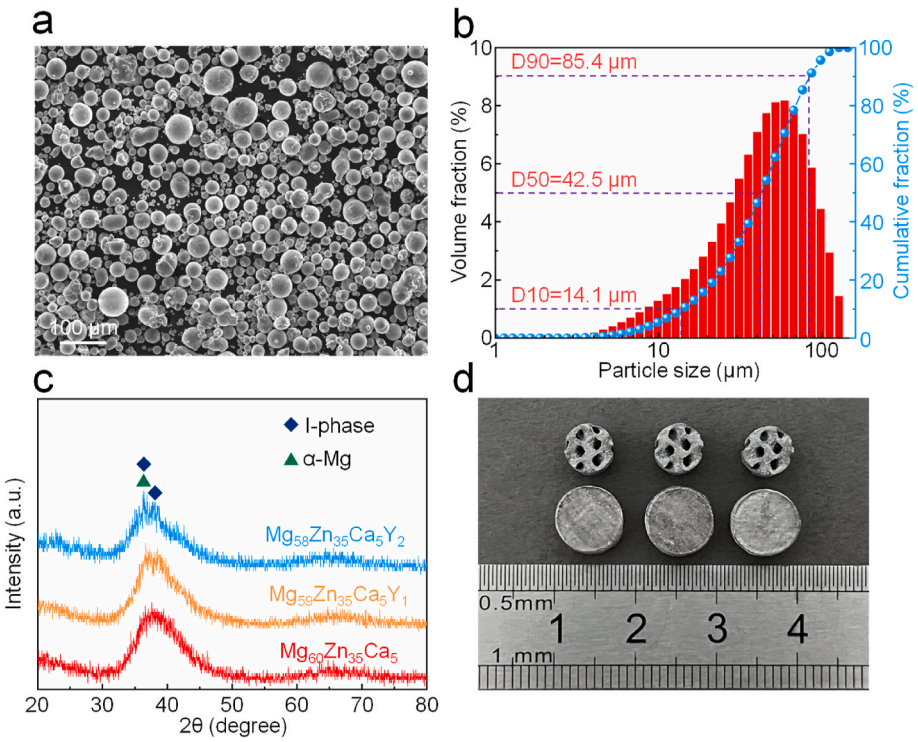

Fig. 1. (a) Morphology, (b) particle size distribution, and (c) XRD pattern of powder. (d) Typical porous and columnar parts prepared by LPBF.

degradation, continuous and dense corrosion layer consisting of Zn oxide/hydroxide and Mg oxide/hydroxide provided excellent protection for substrate. Wang et al. [14] prepared amorphous Mg–Zn–Ag, and found that its corrosion rate was decreased with immersion time increasing, due to the formation of a protective barrier layer with uniform corrosion products. In addition, amorphous Mg alloy also exhibits high strength, as the atoms intertwine with each other and thereby need high energy to tear the matrix [17,18].

From a manufacturing point of view, the preparation of amorphous parts requires a very high cooling rate, so that the atoms have no enough time to arrange orderly during rapid cooling. At present, common preparation methods mainly include water quenching method, spray casting method, copper mold casting method, hot pressing etc. [13,19]. However, the size of the amorphous alloy prepared by above methods is very limited, usually a thin layer structure with a thickness of only a few millimeters. Meanwhile, it is also challenging to obtain a complex porous structure [20,21]. Laser powder bed fusion (LPBF) is a rapid solidification technology, in which the cooling rate ($>10^4$ K/s) is higher than the critical cooling rate (10^3 K/s) required to form the amorphous structure in most amorphous systems. More importantly, LPBF, as a typical additive manufacturing technology, builds parts in a layer-by-layer pattern along the building direction (BD) perpendicular to the substrate. Thus, it can break through the size and shape limitations of conventional preparation methods and prepare large and porous amorphous alloy parts [22–28]. For example, Mahbooba et al. [29] reported that the thickness of iron-based amorphous parts prepared by LPBF could reach 30 mm, which is much higher than the critical dimension of 2 mm for casting. Zhang et al. [30] used LPBF to prepare a zirconium-based amorphous porous scaffold with a porosity of 70 %, a Young's modulus of ~13 GPa, and a yield strength of 350 MPa.

In this work, LPBF was adopted to prepare Mg–Zn–Ca amorphous alloy. Mg–Zn–Ca series alloy was selected owing to its favorable biological properties. It was reported that the released Mg, Zn, and Ca ions could promote bone cell proliferation and differentiation [13,31–33]. Furthermore, considering the intrinsic brittleness of amorphous alloy, rare-earth yttrium (Y) was alloyed with Mg–Zn–Ca, aiming to improve the plastic deformability. Previous research reported that Y addition was able to induce the formation of quasicrystal I-phase (Mg_3Zn_6Y, icosahedral quasicrystal structure) that could tailor the mechanical properties [34–36]. Mg–Zn–Ca based parts with various Y content (0, 1, 2 at.%) were prepared with LPBF. The microstructure, mechanical properties and corrosion behavior were studied comprehensively. Furthermore, the correlation between microstructure and performance was explored in-depth.

2. Materials and methods

2.1. Powder preparation and characterization

The nominal composition (at.%) of raw materials was determined at $Mg_{60}Zn_{35}Ca_5$, $Mg_{59}Zn_{35}Ca_5Y_1$ and $Mg_{58}Zn_{35}Ca_5Y_2$. Aerosolization was utilized to prepare spherical powder. In detail, as-cast alloy was prepared in resistance furnace, then melted and aerosolized under the protection of high purity argon. The as-received $Mg_{60}Zn_{35}Ca_5$ powder was observed by scanning electron microscopy (SEM, Zeiss Sigma-300, Germany), which exhibited favorable sphericity with few satellite particles (Fig. 1a). The particle size was measured using laser particle size analyzer (Mastersizer 3000, Marvin Company, UK). It showed a normal distribution with a d_{10} of 14.1 μm, d_{50} of 42.5 μm and d_{90} of 85.4 μm, as presented in Fig. 1b.

The phase structure of powder was characterized by X-ray diffractometer (XRD, Bruker, D8 Advance, Germany). Typical broad diffraction hump was observed for $Mg_{60}Zn_{35}Ca_5$ powder, indicating its complete amorphous structure (Fig. 1c). It was believed that the atomization process with rapid cooling offered favorable condition for the formation of amorphous structure. For $Mg_{59}Zn_{35}Ca_5Y_1$ and $Mg_{58}Zn_{35}Ca_5Y_2$ powders, several weak crystalline peaks were detected.

2.2. LPBF process

A commercial laser printing system (HBD-150, Guangdong Hanbang 3D Tech Co. Ltd., China) was utilized in LPBF experiments. A fiber laser

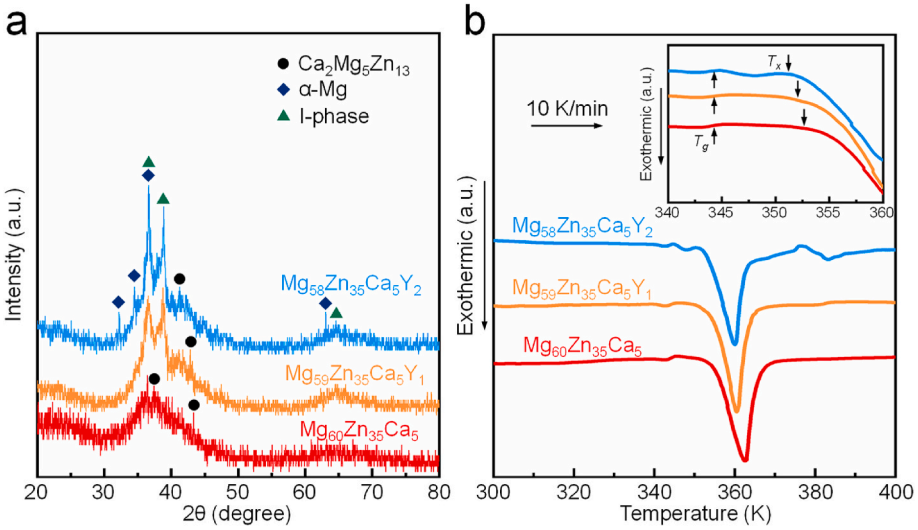

Fig. 2. (a) XRD patterns, and (b) DSC curves of as-built parts. The inset was DSC curve for localized temperature range.

(IPG, 500 W) with a spot of ~70 μm was applied as heat source. During LPBF, the processing chamber was filled with high purity argon to avoid oxidation. It is well accepted that Mg powder easily evaporates under the irradiation of high-energy laser beams. Herein, a gas circulation device was used to remove Mg fume, aiming to mitigate its negative impact on processing. After a series of pre-experiments, the parameters were optimized at laser power 85 W, scanning rate 130 mm/s, hatch space 60 μm and layer thickness 50 μm. Typical porous and columnar parts were exhibited in Fig. 1d.

2.3. Microstructural characterization

The phase structure of as-built part was investigated by XRD. The glass transition and crystallization behavior were studied using differential scanning calorimetry (DSC, ZBDSC-2D, Beijing Hengjiu Science Instrument Factory, China) at a heating rate of 10 K/min.

To reveal microstructure, the as-built part was sequentially grounded using 600, 1200 and 2000 SiC papers, then mechanically polished to obtain mirror surface, and etched using 3 vol% nitric acid alcohol solution. The microstructure was observed using SEM in backscattered electron mode. Furthermore, the part was grounded to 40 μm thickness, punched into small discs with a diameter of 3 mm, and then thinned with an ion thinner (Gatan 691, Gatan, USA). Nano-scaled microstructure was captured by using a transmission electron microscopy (TEM, Tecnai G2 F20, FEI Company, USA).

2.4. Mechanical testing

The as-built part was cut in parallel using a wire cutting machine. Uniaxial compression test was carried out using a conventional mechanical testing machine (E44.304, Metes industrial systems Co. Ltd., China) at 5×10^{-4} s^{-1}. Subsequently, the lateral and fracture surface were captured utilizing SEM. Nanoindentation test was performed via Nano indenter (G200, Agilent, USA) at a constant strain rate of 0.05 s^{-1} and depth of 200 nm. In addition, TEM and SEM analysis were carried out on the samples after 2 % compression strain to study deformation mechanism.

2.5. Electrochemical testing

Electrochemical test was implemented to study the corrosion behavior of as-built part and the stability of its surface corrosion product layer by using an electrochemical workstation (PARSTAT 4000A, Princeton Applied Research, USA) with three classical electrodes, including working electrode, counter electrode and reference electrode. Prior to test, the part was ground and polished, then soldered to copper wire and wrapped with epoxy resin leaving an exposure area (1 cm^2). Subsequently, the part was immersed in simulated body fluid (SBF, pH 7.4) for 7 d so that its surface was completely covered with corrosion products. Open circuit potential (OCP) measurement was performed for half an hour. Electrochemical impedance spectroscopy (EIS) test was performed from 10^5 to 10^{-2} Hz, then analyzed and fitted via ZSimpDemo 3.30 software. Potential dynamic polarization (PDP) test was carried out within OCP±500 mV at 1 mV/s. Based on Tafel extrapolation method, corrosion potential (E_{corr}) and corrosion current density (i_{corr}) were determined from the PDP curves.

2.6. Immersion test

Immersion experiment was performed in SBF for 28 d at 37 °C, with the ratio of corrosive solution volume to exposure sample area (100 mL/cm^2) [37]. The generated hydrogen was collected through funnel into 25 mL inverted burette and recorded. During immersion, the solution was renewed every one day. The corrosion rate was calculated by hydrogen evolution (P_H, mm/year) [38]:

$$P_H = 2.088\frac{V_H}{At} \quad (1)$$

where V_H (mL) was hydrogen evolution volume, A (cm^2) was exposed surface area and t (day) was immersion time. After 28 d, the part was dried in air. The corrosion surface and cross section were treated with gold spray and observed by SEM. Chromic acid solution (200 g/L CrO_3 and 10 g/L $AgNO_3$) was chosen to removing corrosion products. Subsequently, the corrosion surface without products was observed via SEM. The mass loss (W, mg) was measured and corresponding corrosion rate (P_w, mm/year) was calculated:

$$P_W = 2.10\frac{W}{At} \quad (2)$$

2.7. In vitro biocompatibility assessment test

Mouse cranial preosteoblasts (MC3T3-E1) were adopted for in vitro cell test. Sterilized part was immersed in Dulbecco modified Eagle medium (DMEM) that contained 10 % fetal bovine serum for 3 d to obtain extracts. The ratio of medium volume to exposure sample area was set at 0.8 mL/cm^2 from ISO 10993-5: 2009 standard [7]. Cells at a density of 5000 cells/well were planted in 96 well plates, and then incubated for 1

Table 1
Thermal characteristics from DSC curves, showing the glass transition temperature (T_g), the crystallization temperatures (T_x), the undercooled liquid region ($\Delta T = T_x$-T_g), and the crystallization enthalpy (ΔH_{cryst}).

Parts	T_g (K)	T_x (K)	ΔT (K)	ΔT_{cryst} (J/g)
$Mg_{60}Zn_{35}Ca_5$	344.1	354.7	10.6	56.4
$Mg_{59}Zn_{35}Ca_5Y_1$	344.3	353.2	8.9	34.3
$Mg_{58}Zn_{35}Ca_5Y_2$	344.2	351.6	7.5	25.7

d. Afterwards, the extracts were added to replace the medium and renewed every 2 d. After incubating for 1, 4, and 7 d, cell counting Kit-8 (CCK-8) reagent of 10 μL was added to further culture for 1 h. The absorbance was determined via a microplate reader (Beckman, USA) at 450 nm. The cell viability was calculated by:

$$\text{Cell viability } (\%) = OD_{part}/OD_{blank} \times 100\%$$

In addition, the live/dead cell assay was carried out, in which the cells were stained and visualized using Calcein-AM and Ethidium homodimer-1 reagents for 30 min. The cell morphology was captured utilizing a fluorescence microscope (BX60, Olympus Co., Japan).

2.8. Statistical analysis

All tests were executed at least three times to guarantee the reliability. The data were represented as mean ± standard deviation. The statistical significance was determined using one-way analysis of variance (ANOVA) by Tukey's test. Herein, p value less than 0.05 was believed to be of statistical significance.

3. Results and discussion

3.1. Microstructural characteristics

The phase structure of as-built parts was examined by XRD, with results depicted in Fig. 2a. In general, a specific broad diffraction hump ranging from 30 to 50° was observed for all parts, which clearly revealed their amorphous structure. Several weak crystal diffraction peaks were also detected, indicating the occurrence of crystallization behavior during LPBF. The α-Mg and $Ca_2Mg_5Zn_{13}$ phase were major crystallization phase in $Mg_{60}Zn_{35}Ca_5$ part. Notably, their diffraction peaks gradually turned strong with Y increasing, while new crystallization peaks corresponded to quasicrystal I-phase appeared. The thermodynamic stability was investigated utilizing DSC, with collected curves shown in Fig. 2b. Moreover, the corresponding thermal characteristics were listed in Table 1 and comparable to those of reported studies on Mg-based amorphous alloys [39–41]. All scanning curves exhibited an endothermic signal associated with the glass transition, as indicated by the arrow at ~344 °C in Fig. 2b, which reaffirmed the formation of glassy atomic structure. Besides, exothermic crystallization peaks corresponding to the start of crystallization were also detected. Notably, Y addition reduced the crystallization temperatures (T_k) in some extent,

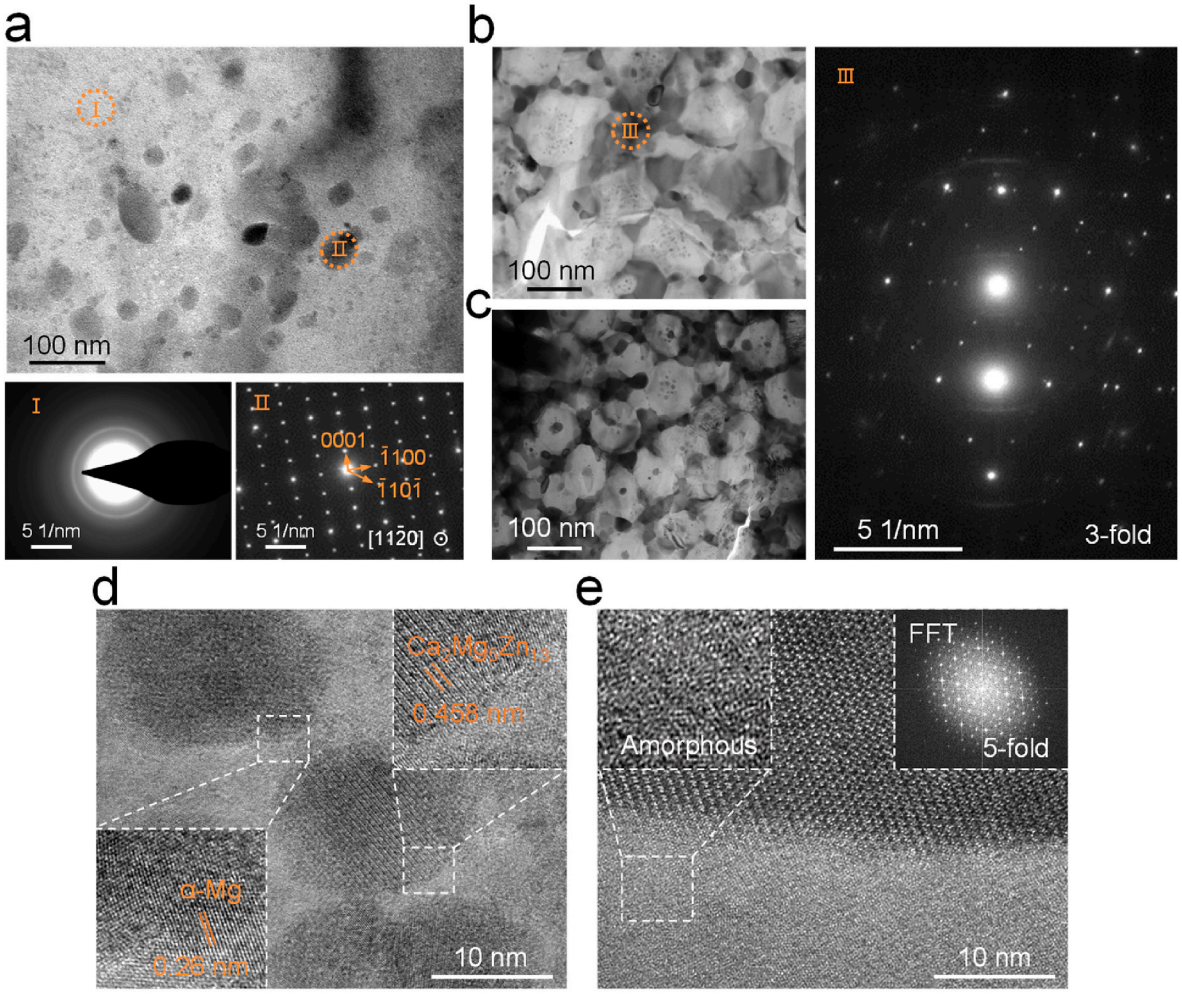

Fig. 3. TEM and SAED patterns of (a) $Mg_{60}Zn_{35}Ca_5$, (b) $Mg_{59}Zn_{35}Ca_5Y_1$ and (c) $Mg_{58}Zn_{35}Ca_5Y_2$ parts. HR-TEM and FFT patterns of (d) $Mg_{60}Zn_{35}Ca_5$ and (e) $Mg_{59}Zn_{35}Ca_5Y_1$ part.

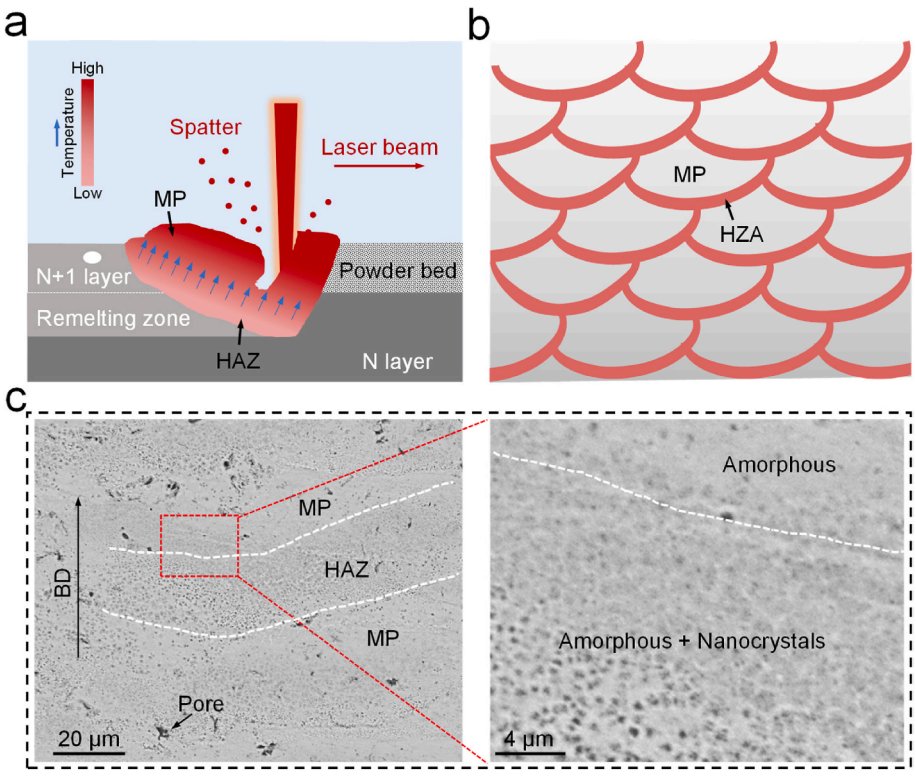

Fig. 4. (a) Schematic diagram of laser melting process, in which the direction of temperature gradient is from the edge (low) of molten pool to its center (high), (b) hierarchical microstructure in as-built part and (c) SEM showing the cross-section microstructure of as-built $Mg_{60}Zn_{35}Ca_5$ part.

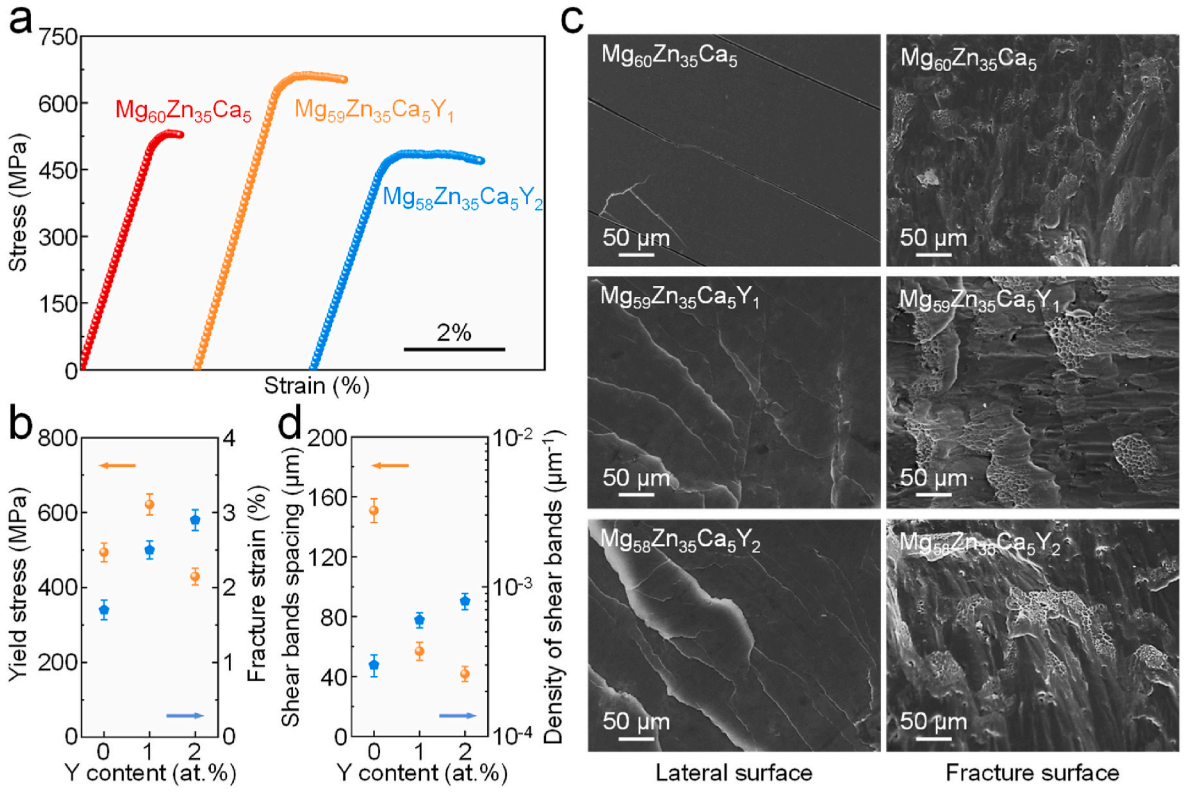

Fig. 5. (a) Compressive stress-strain curves, and (b) corresponding mechanical parameters. (c) Lateral and fracture surface morphologies, and (d) shear band spacing and density of fractured parts.

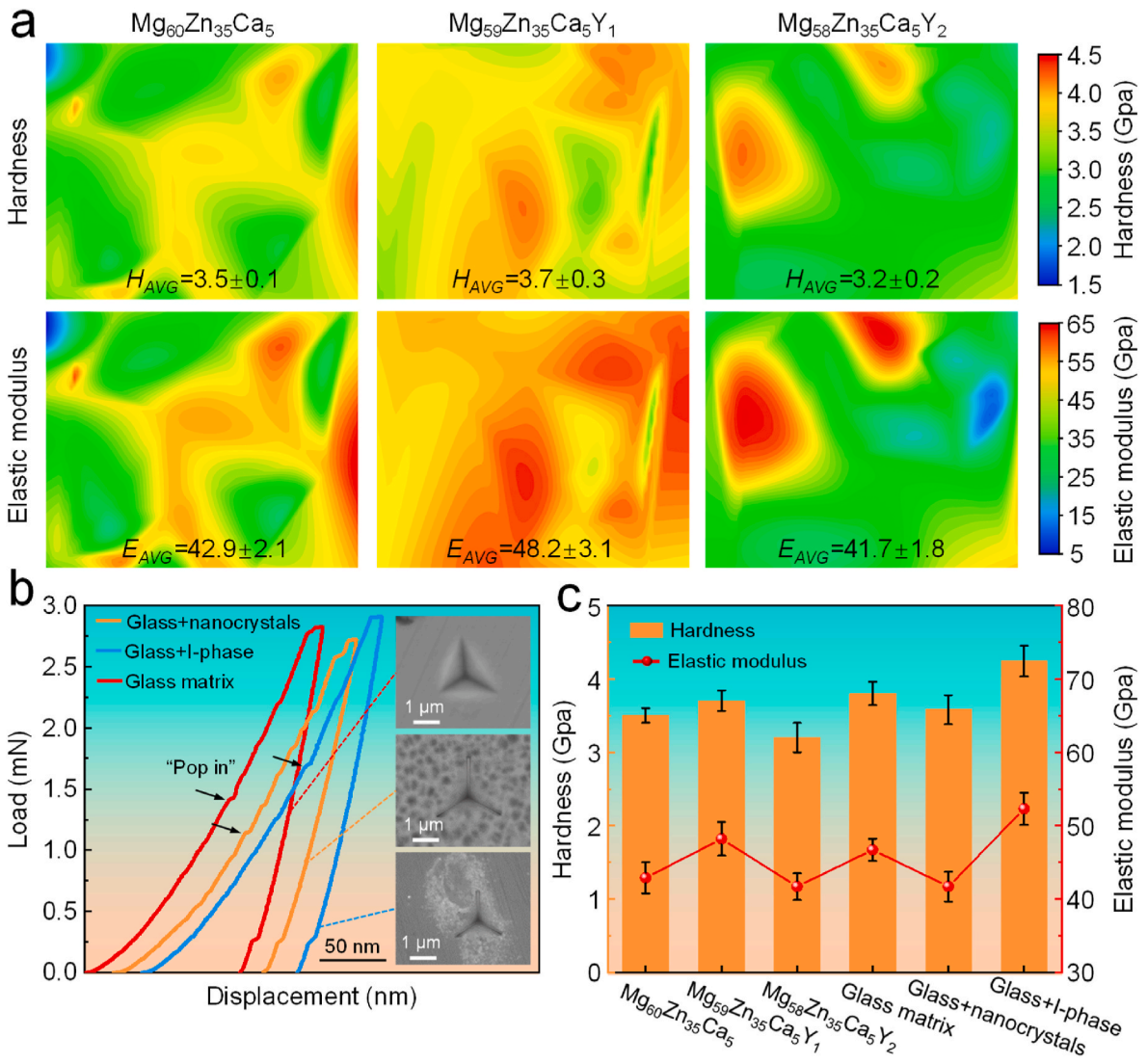

Fig. 6. Nanoindentation analysis: (a) hardness maps, elastic modulus maps, (b) load-displacement curves, and (c) hardness and modulus. The inset was the position of indentation, while nanocrystals were α-Mg and $Ca_2Mg_5Zn_{13}$ phases.

since it deteriorated the thermal stability of amorphous structure. Moreover, the crystallization enthalpies (ΔH_{cryst}) gradually decreased due to the enhanced crystallization, namely, the increased crystal volume fraction.

TEM was executed to explore the microstructure in-depth, with bright-field (BF) images and selected area electron diffraction (SAED) patterns shown in Fig. 3. For $Mg_{60}Zn_{35}Ca_5$ part, some nanocrystals (~30 nm) were observed in matrix (Fig. 3a). From the SADF image, the matrix (Region I) exhibited a typical electron diffraction pattern of halo ring, which confirmed its amorphous structure. The nanocrystal (Region II) was identified as α-Mg with close-packed hexagonal structure [42]. After Y addition, the numbers and volume fraction of crystalline phases were considerably increased (Fig. 3b-c). Numerous striated crystalline phases tended to form rings in $Mg_{59}Zn_{35}Ca_5Y_1$ part. The corresponding SADF pattern (Region III) presented typical 3-fold rotational symmetry, which confirmed its icosahedral quasicrystal structure. As Y increased to 2 at. %, ring-like crystalline phases formed a continuous network-like distribution. High resolution TEM (HR-TEM) further proved the formation of amorphous structure with disordered atomic arrangement, quasicrystals with unique 5-fold rotational structure, as well as α-Mg (0.26 nm), $Ca_2Mg_5Zn_{13}$ (0.458 nm) phase from their crystal plane spacing (Fig. 3d–e) [15,43,44]. Besides, the amorphous matrix and in-situ precipitated crystalline phase were tightly integrated, showing a favorable bonding interface.

The above microstructure analysis revealed that crystallization behavior occurred, which was usually considered an inevitable phenomenon during LPBF. As schematically showed in Fig. 4a and b, the as-built parts generally consisted of two regional structures, namely melt pool (MP) and heat-affected zone (HAZ). Herein, MP was formed by a high energy laser beam radiating onto the surface of the powder bed causing the powder to melt. HAZ was the reheating region between overlapping melt pools and where the current layer (N+1) melt pool reheated the previous layer of deposition (N) [45,46]. Therefore, the two regions undergone different heat history and consequently exhibited hierarchical microstructure. As shown in Fig. 4c, two distinct stratified regions could be clearly observed along the building direction of $Mg_{60}Zn_{35}Ca_5$ part. The smooth region corresponded to the melt pool was usually a monolithic glass since it experienced an extremely high cooling rate. Distinctively, the HAZ partially crystallized (the glass and crystalline phase coexisted). It was believed that temperature of HAZ was relatively low, but still higher than the crystallization temperature, which induced the transformation of the amorphous structure into a crystalline structure, also known as structural relaxation [22,47].

On the other hand, the physicochemical properties of powder composition also affected the crystallization behavior. In theory, amorphous alloys need to contain more than three components with

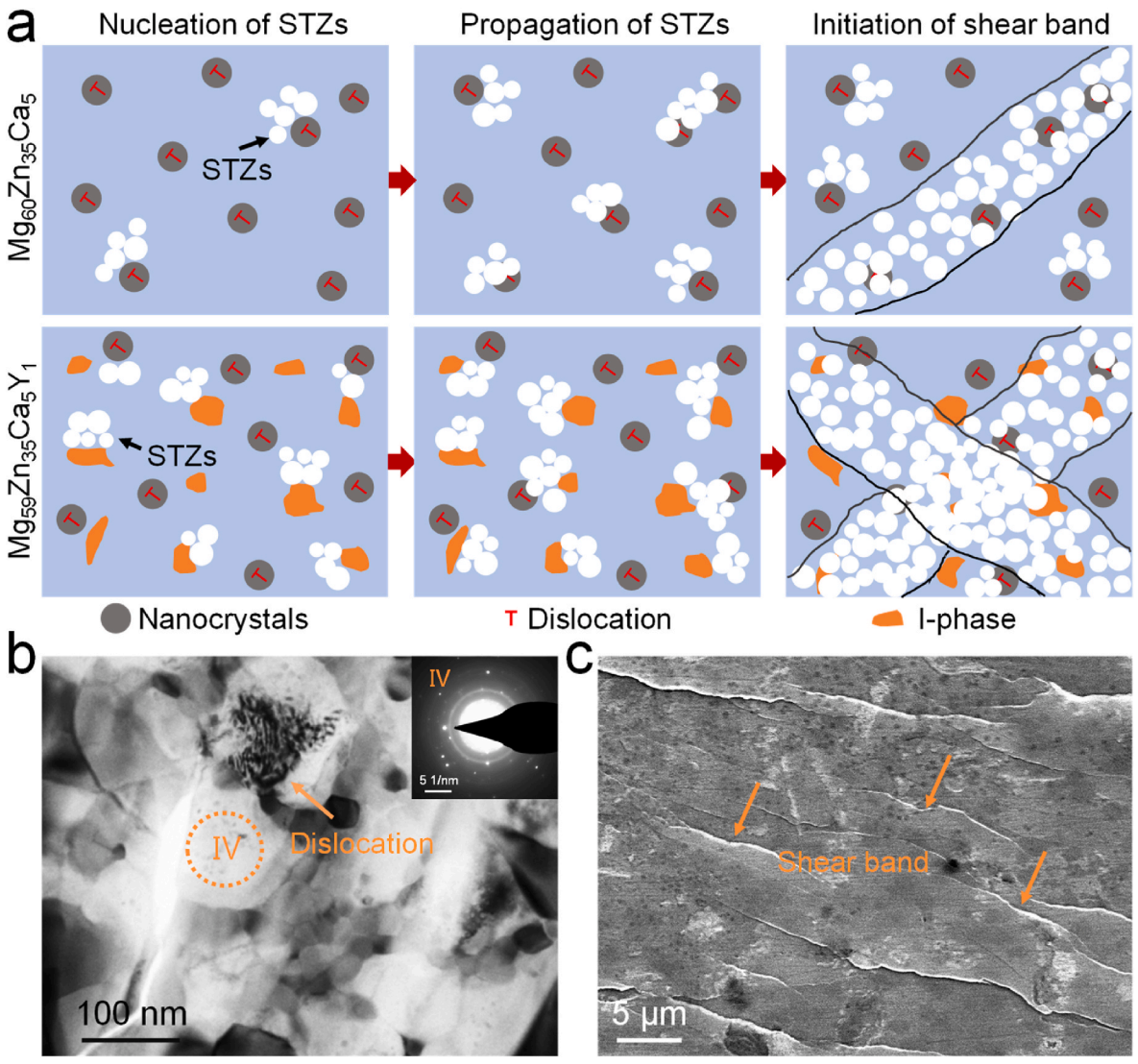

Fig. 7. (a) Deformation process of $Mg_{60}Zn_{35}Ca_5$ and $Mg_{59}Zn_{35}Ca_5Y_1$ part, in which I-phase is the quasicrystal. (STZs, small clusters of atoms which rearrange themselves spontaneously and cooperatively under shear stress, is a fundamental unit of shear band formation [50].) (b) TEM of dislocation from nanocrystals, SADF pattern for the coexistence of glass matrix with nanocrystals and (d) multiple shear bands of deformed $Mg_{59}Zn_{35}Ca_5Y_1$ part subjected to a compression strain of 2 %.

large atomic size differences (>12 %) and negative mixing enthalpy [48]. Previous researches proved the favorable glass forming ability of $Mg_{60}Zn_{35}Ca_5$ ternary system [15]. In our work, the alloy treatment with Y promoted the crystallization, particularly the formation of I-phase. A coincident fact was that the composition domain to generate I-phase in Mg–Zn–Y ternary system was similar to that for the formation of amorphous structure in Mg–Zn–Ca ternary system. That was 60–75 at.% of Mg, 25–40 at.% of Zn, and less than 6 at.% of Y or Ca [34]. Nevertheless, the formation of I-phase demanded no strict requirements for cooling rate. Meanwhile, the crystallization temperature of I-phase was above the glass transition temperature [49]. Thus, in $Mg_{59}Zn_{35}Ca_5Y_1$ quaternary system, 1 at.% of Y addition preferentially consumed Mg and Zn atoms to form I-phase, thereby ruining the original glass forming ability of Mg–Zn–Ca ternary system. However, in $Mg_{58}Zn_{35}Ca_5Y_2$ system, the total content Y and Ca was above 6 at.%. In terms of atomic composition ratio, it provided convenience for the formation of other crystalline phases, like α-Mg. As showed in Fig. 2a, the obvious diffraction peaks of α-Mg confirmed this point.

3.2. Mechanical properties

The typical compressive stress-strain curves were depicted in Fig. 5a, and corresponding mechanical parameters were exhibited in Fig. 5b. All parts exhibited extremely high yielding strength, but relatively insufficient plastic deformation ability due to their intrinsic amorphous characteristic. Particularly, $Mg_{60}Zn_{35}Ca_5$ part exhibited a fracture strain of 1.7 % and a yield strength of 493.7 MPa. Notably, 1 at.% Y addition increased the strain to 2.5 %, and yield strength to 621.3 MPa. However, continuous Y addition unfriendly reduced the yield strength to 429.2 MPa, despite the further improvement of deformation ability. The lateral and fracture morphologies of post-test parts were captured by SEM, as showed in Fig. 5c. For all parts, secondary shear bands leading to shear offsets could be detected on the lateral surfaces, and the number of shear bands increased with Y addition. Meanwhile, the shear band spacing decreased from~151 μm to ~42 μm (2 at.% Y), whilst the shear band density increased from $\sim 3 \times 10^{-4}$ μm^{-1} to $\sim 8 \times 10^{-4}$ μm^{-1}, implying that more local plastic regions were activated after Y addition (Fig. 5d). Another feature of the plastic deformation, vein pattern, was also found on the fracture surfaces. In general, the fracture surface morphology of $Mg_{59}Zn_{35}Ca_5$ part was mainly composed of smooth areas, which was the result of shear deformation that occurs before fracture. For $Mg_{59}Zn_{35}Ca_5Y_1$ and $Mg_{58}Zn_{35}Ca_5Y_2$ part, the fractured surface exhibited more vein pattern features, which also confirmed their improved plasticity.

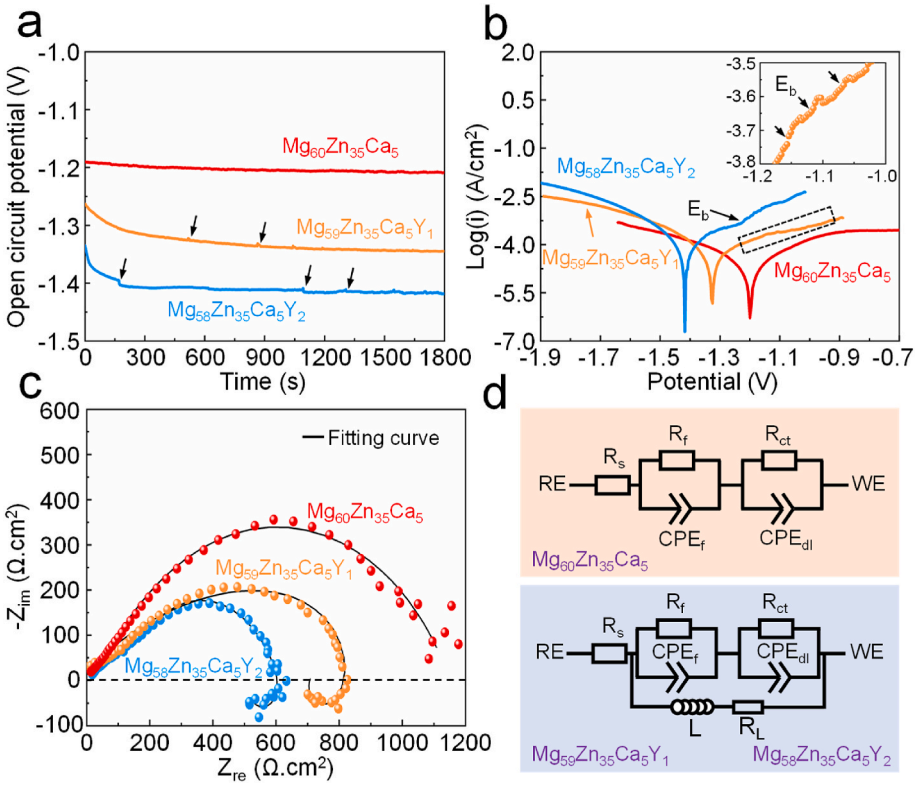

Fig. 8. (a) OCP, (b) PDP curves, (c) Nyquist and (d) equivalent circuits obtained by electrochemical testing.

Table 2
Electrochemical parameters from PDP curves and equivalent circuits.

Parts	i_{corr} (μA/cm^2)	E_{corr} (V)	R_f (Ω·cm^2)	R_{ct} (Ω·cm^2)	L (H·cm^2)	R_L (Ω·cm^2)
$Mg_{60}Zn_{35}Ca_5$	39.0 ± 1.4	−1.15 ± 0.01	124.3 ± 32.5	1192 ± 52.3	/	/
$Mg_{59}Zn_{35}Ca_5Y_1$	53.7 ± 3.2	−1.32 ± 0.03	102.9 ± 25.3	619.1 ± 32.1	34750 ± 223	3956 ± 102
$Mg_{58}Zn_{35}Ca_5Y_2$	107.2 ± 5.3	−1.42 ± 0.02	63.4 ± 18.5	541.2 ± 22.6	16830 ± 153	2153 ± 83

Nanoindentation test was performed, with microhardness and elastic modulus maps shown in Fig. 6a. The color ranging from blue to red corresponded to gradually improved hardness and modulus. It could be seen that $Mg_{59}Zn_{35}Ca_5Y_1$ part was dominated with red areas, and exhibited relatively high H_{AVG} (3.7 ± 0.3 GPa) and E_{AVG} (48.2 ± 3.1 GPa). However, $Mg_{58}Zn_{35}Ca_5Y_2$ part exhibited smallest H_{AVG} (3.2 ± 0.2 GPa) and E_{AVG} (41.7 ± 1.8 GPa) among the three groups. In addition, the load-displacement curves obtained at specific areas with various phase combination were studied, as depicted in Fig. 6b. A sharp 'pop-in' (abrupt increase in indentation displacement) was visible on all the curves, corresponding to the initial yield point. As compared with glass matrix, (glass + nanocrystals) presented a premature yield point (a decreased yield load) and reduced hardness and modulus, which indicated α-Mg phase and $Ca_2Mg_5Zn_{13}$ were soft phases with low hardness and modulus. However, I-phase precipitation lagged the yield point and increased the yield load, hardness and modulus, which indicated that I-phase could act as a hard phase. Therefore, the as-built $Mg_{59}Zn_{35}Ca_5Y_1$ part with I-phase presented improved hardness, elastic modulus and yield strength (Fig. 6c). Notably, $Mg_{58}Zn_{35}Ca_5Y_2$ part owned further increased crystallized phase (α-Mg), which weakened the strengthening effect of I-phase.

Our results clearly proved that Y addition tailored the mechanical properties of LPBF processed Mg–Zn–Ca amorphous alloy, which should be correlated with the different type and quantity of crystalline phases in glass matrix. For complete amorphous alloy, it has almost no clear plastic deformation zone. For example, Zhao et al. [34] prepared monolithic $Mg_{71}Zn_{25}Ca_4$ amorphous alloy with only a linear elastic behavior and no plastic deformation. For $Mg_{60}Zn_{35}Ca_5$ part presented in this work, the compressive test proved it included elastic deformation and a small amount of plastic deformation. As revealed by previous TEM observation, there were very small amount of nano-scaled crystalline phases (α-Mg and $Ca_2Mg_5Zn_{13}$) in $Mg_{60}Zn_{35}Ca_5$ part. Under the effect of external stress, the phases with low hardness and modulus acted as soft phases and preferentially yielded. Due to the mismatch in modulus, stress concentration occurred at the phase-amorphous interface, leading to the phases deformation by inducing the formation of dislocation (T). Subsequently, these deformed phases acted on the surrounding amorphous matrix to stimulate the nucleation and then propagation of the STZs, ultimately achieving the initiation of shear band slip systems. (Fig. 7a). Thus, the $Mg_{60}Zn_{35}Ca_5$ part in this work still showed small plastic deformation areas. With Y content increasing, the crystalline phases were significantly increased, which effectively improved the plastic deformation ability. In theory, the improvement of plasticity would undoubtedly sacrifice a certain amount of strength, like $Mg_{58}Zn_{35}Ca_5Y_2$ part. However, the $Mg_{59}Zn_{35}Ca_5Y_1$ part showed simultaneously improved strength and plasticity as compared with the other two groups. As our nanoindentation tests revealed, quasicrystal I-phase owned higher hardness and modulus than the glass matrix. Thus, the I-phase in $Mg_{59}Zn_{35}Ca_5Y_1$ part served as hard and reinforced particles, whose surrounding glass matrix yielded preferentially as subjected to high external forces. Consequently, the activation of shear band slip in $Mg_{59}Zn_{35}Ca_5Y_1$ consumed more fracture energy, which gave birth to

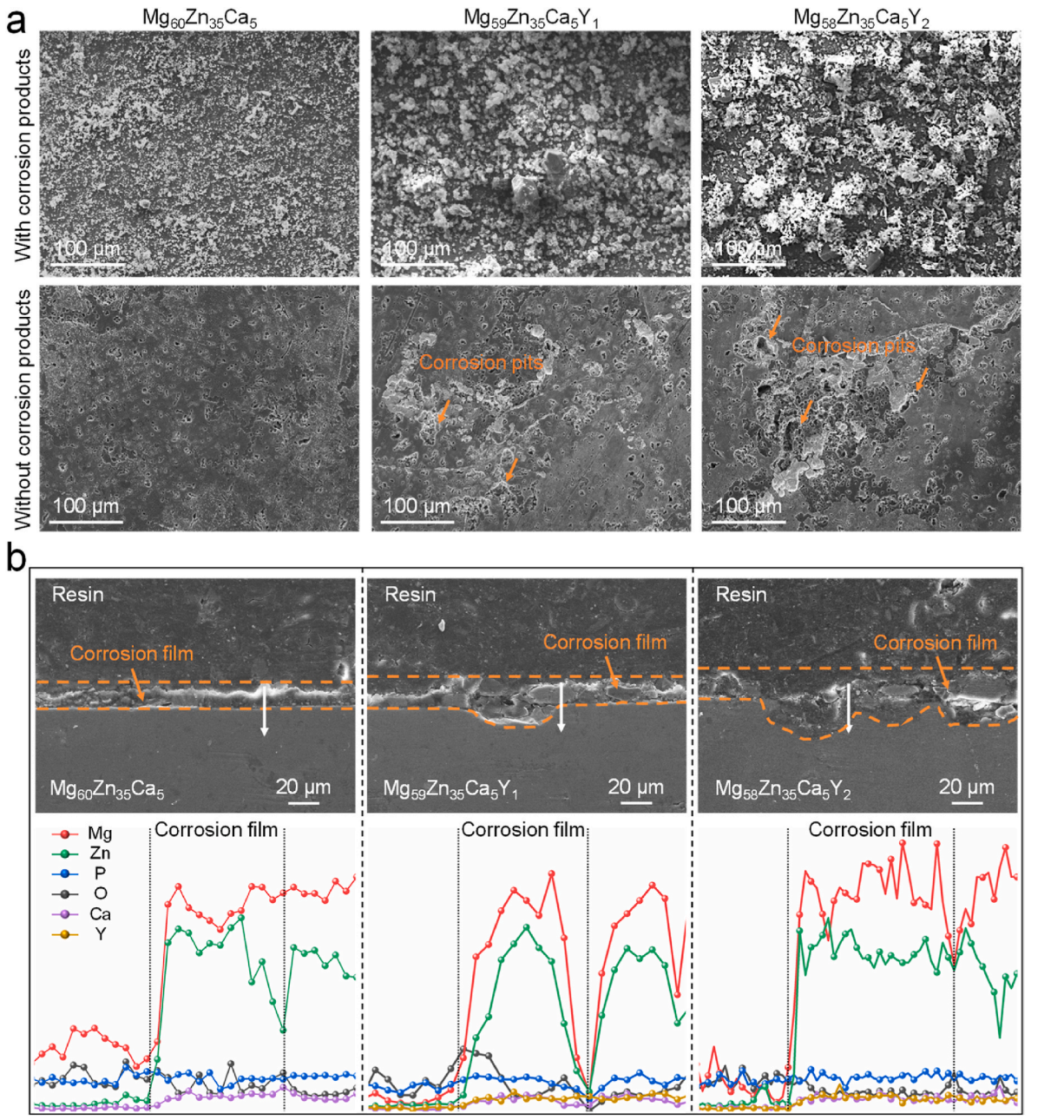

Fig. 9. (a) Corrosion surface with and without corrosion products, (b) cross-section morphology and EDS line scan of corrosion products layer.

high yielding strength. On the other hand, I-phase as hard phases could also hinder the movement of shear band and induce the generation of secondary shear bands [34]. As showed in Fig. 7c, it also was clearly observed that shear band proliferated at the I-phase/glass matrix interface. In short, our work revealed that suitable Y alloying could bring about positive impacts of mechanical properties for laser printed Mg–Zn–Ca amorphous alloy.

3.3. Corrosion behavior

The corrosion behavior was investigated using electrochemical experiments, with recorded OCP curves plotted in Fig. 8a. Initially, the potential of all parts shifted to low potential due to the dissolution of corrosion products, and then varied dynamically in equilibrium [51]. Herein, $Mg_{60}Zn_{35}Ca_5$ part exhibited a high potential of ~ −1.21 V. After Y addition, the parts displayed a rapidly decreased potential, indicating unstable corrosion layer and resultant peeling. Meanwhile, the sudden fluctuations in potential could be detected, which revealed the occurrence of pitting. The PDP curves were depicted in Fig. 8b, and the E_{corr} and i_{corr} were listed in Table 1. It was revealed that Y alloying decreased the E_{corr} and improved the cathodic polarization current. Breakdown potentials (E_b) were evidently found in their anodic polarization curves, which was an indication of localized corrosion.

Nyquist plots obtained by EIS tests were depicted in Fig. 8c. All parts contained two characteristic capacitance loops at high and medium frequencies. After Y addition, the capacitance ring turned small, indicating low charge transfer resistance. More importantly, the inductive loop appeared at low frequency, which was a signal of corrosion product layer collapse and localized corrosion. Therefore, two corresponding equivalent circuits were fitted, as displayed in Fig. 8d. The R_s was the solution resistance. The R_f and CPE_f were defined as the resistance and capacitance of corrosion product layer. The R_{ct} and CPE_{dl} were defined as the charge transfer resistance and double layer capacitor on sample substrate surface, respectively. The R_L and L represented the resistance

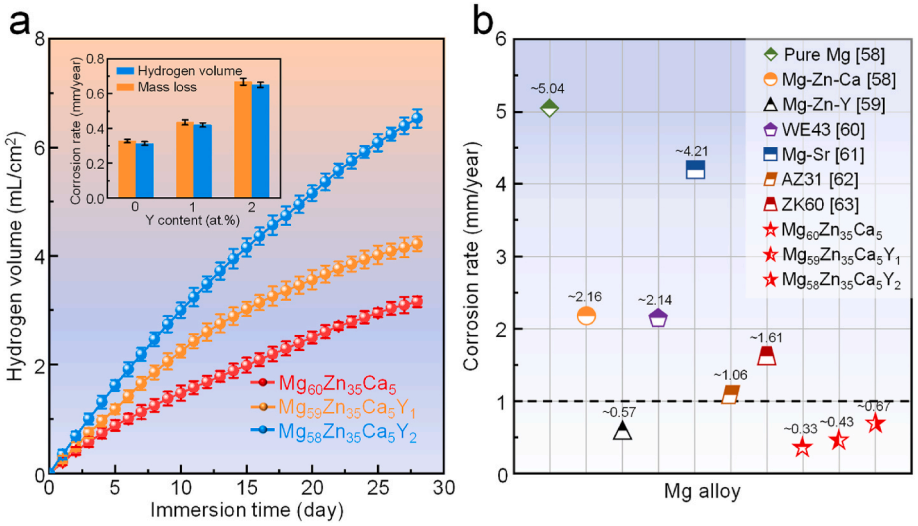

Fig. 10. (a) H_2 variation and degradation rate. (b) Comparison of corrosion rate (mass loss) among as-builts parts as well as reported bio-degradable Mg alloys in SBF (PH 7.4) at 37 °C (Pure Mg [58], Mg-Zn-Ca [58], Mg–Zn–Y [59], WE43 [60], Mg-Sr [61], AZ31 [62], ZK60 [63]).

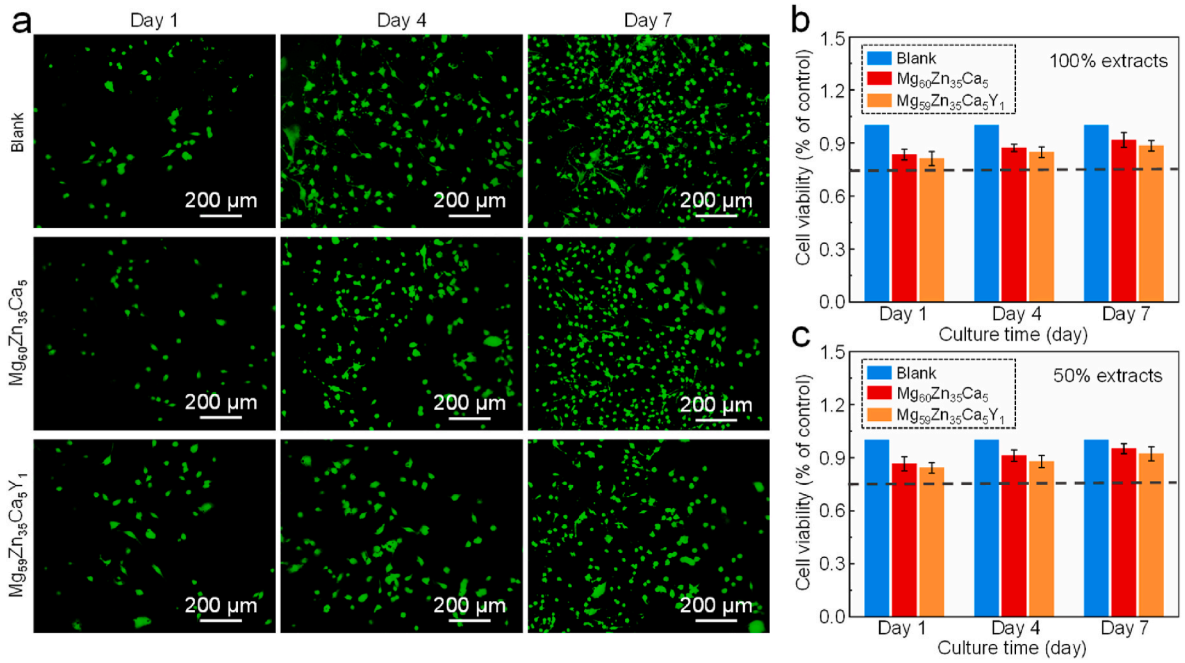

Fig. 11. (a) Fluorescence microscopy images of MC3T3-E1 cells cultured in 100 % extracts for 1, 4 and 7 d, (b) cell viabilities in 50 % and 100 % extracts.

and inductance from the collapse of partial corrosion layer in response to Mg^{+} reaction. As listed in Table 2, Y-containing parts presented low R_{ct} and R_f, which indicated that Y addition promoted the charge transfer and destabilized the protective layer, thus weakening the corrosion resistance.

Immersion test was performed to further explore the biodegradation behavior, with biodegradation surface exhibited in Fig. 9a. All parts were completely covered with corrosion products. Particularly, dense and flat corrosion layer covered on $Mg_{60}Zn_{35}Ca_5$ part, whereas the parts with Y possessed loose and granular corrosion products. Some studies reported that the granular was $CaCO_3$ (high $K_{SP} = 4.9 \times 10^{-9}$), indirectly reflecting their relatively fast corrosion rate to produce more Ca^{2+} [52, 53]. The corrosion morphologies after removing product clearly revealed that the parts with Y experienced local corrosion, as proved by the large corrosion pits. In contrast, the $Mg_{60}Zn_{35}Ca_5$ part was corroded relatively slightly and uniformly. In addition, the cross-section of product layer was observed via SEM, as shown in Fig. 9b. The corrosion film of $Mg_{60}Zn_{35}Ca_5$ part was only about 10 μm thick and uniformly covered the matrix. However, for the parts with Y, the corrosion film reached a thickness of ~15–20 μm. Furthermore, the obvious localized corrosion pits could be detected. Also, $Mg_{58}Zn_{35}Ca_5Y_2$ part experienced a more severe localized corrosion than $Mg_{59}Zn_{35}Ca_5Y_1$. From EDS line analysis, Zn elements were detected in all corrosion product layers, which indicated the formation of Zn oxide/hydroxide. For the parts with Y, EDS line analysis next to corrosion pits confirmed the presence of Y oxide/hydroxide, which could be related to the galvanic corrosion constituted between I-phase and substrate. In addition, Ca and P elements were also detected, which indicated Ca–P products like (apatite) deposited on the matrix.

The H_2 volume variation during immersion test was depicted in Fig. 10a. The $Mg_{60}Zn_{35}Ca_5$ part showed slowest hydrogen volume evolution among all groups. After Y addition, the parts exhibited an

increased hydrogen release rate, namely accelerated corrosion rate. Accordingly, $Mg_{59}Zn_{35}Ca_5Y_1$ showed an accelerated corrosion rates of 0.43 mm/year. A comparison between the degradation rate of amorphous and polycrystalline Mg alloys were exhibited in Fig. 10b. There was no doubt that the amorphous Mg alloys showed relatively low corrosion rate than polycrystalline Mg alloys. As is well known, grain boundaries are usually the beginning of corrosion, as atoms from grain boundaries typically have higher energy and are most sensitive to corrosion [54]. At the same time, the precipitated phase is easy to construct a micro couple with the Mg matrix, as different phase compositions often have potential differences [55]. Notably, the matrix of $Mg_{60}Zn_{35}Ca_5$ was mainly amorphous, as showed in Fig. 3a. There were very few of grain boundaries, dislocations, and other factors that could easily lead to corrosion. Thus, it ultimately achieved a uniform and slow degradation. In fact, the dense and uniform passivation film also confirmed its uniform degradation model. However, the parts with Y were relatively crystallized. A large number of crystalline phases, including α-Mg, $Ca_2Mg_5Zn_{13}$ and quasicrystal I-phase, would form localized galvanic corrosion with the surrounding amorphous Mg matrix, while the same corrosion would also occur between them. In addition, the SBF with high concentrations of chloride ions can easily break through the corrosion product layer, leading to rapid expansion of initial corrosion pits and ultimately leading to the collapse of the matrix. As exhibited in Fig. 9a, unevenly distributed and deep corrosion pits appeared, which clearly confirmed this localized corrosion mechanism. Despite this, the corrosion rate of $Mg_{59}Zn_{35}Ca_5Y_1$ part was less than 0.5 mm/year, which still met the clinical corrosion requirement for orthopaedic implants [56,57].

3.4. *In vitro biocompatibility assessment*

In term of above results, the biocompatibility of $Mg_{60}Zn_{35}Ca_5$ and $Mg_{59}Zn_{35}Ca_5Y_1$ parts were evaluated, with a blank control group. The fluorescence microscopy images of MC3T3-E1 cells were captured, as presented in Fig. 11a. Herein, live cells were green and dead cells were red. Notably, almost no dead cells were visible during the entire culture, while the live cell number increased with incubation time. As compared with the blank group, the $Mg_{60}Zn_{35}Ca_5$ and $Mg_{59}Zn_{35}Ca_5Y_1$ groups possessed relatively few cells number, due to the relatively high corrosive ion solubility in the extracts. CCK-8 assay was carried out to quantitatively assess cell viabilities (Fig. 11b–c). Apparently, the cell viabilities for both two groups increased with incubation time, but $Mg_{59}Zn_{35}Ca_5Y_1$ group exhibited relatively low cell viabilities. This could be due to the fact that the alloy with higher corrosion rate increased the pH and osmotic pressure in the medium, which is obviously not conducive to cellular proliferation [64]. In detail, the cell viabilities for $Mg_{60}Zn_{35}Ca_5$ were 91.7 % after 7 d, but dropped to 88.4 % for $Mg_{59}Zn_{35}Ca_5Y_1$. Moreover, the diluted extracts (50 %) provided a better environment for cell proliferation than 100 % extracts. Based on standard (ISO 10993–5:1999) [65], the biosafety was assessed as grade 0–1 in 50 % and 100 % extracts, which was acceptable for the clinical requirement.

4. Conclusions

In this study, Mg–Zn–Ca and Mg–Zn–Ca–Y amorphous parts were successfully fabricated by LPBF. Their microstructure, mechanical properties, corrosion behavior and biocompatibility were studied. The conclusions were as follows:

(1) As-built parts contained amorphous structure, despite that a few nano-sized crystallized phases (α-Mg and $Ca_2Mg_5Zn_{13}$) were found in glass matrix due to repeated heat accumulation in HAZs. More importantly, Y alloying ruined the glass forming ability and stimulated the in-situ formation of quasicrystal I-phase.

(2) As compared with $Mg_{60}Zn_{35}Ca_5$ part, $Mg_{59}Zn_{35}Ca_5Y_1$ exhibited simultaneously enhanced strength and plasticity. This was because I-phase as a hard phase retarded the propagation of shear bond and thus excited the emergence of secondary shear bands and vein patterns.

(3) $Mg_{60}Zn_{35}Ca_5$ part with few crystalline defects achieved a uniform and slow degradation. The parts with Y possessed loose corrosion layers and exhibited reduced corrosion resistance. Despite this, $Mg_{59}Zn_{35}Ca_5Y$ part still presented moderate corrosion rate of 0.43 mm/year.

(4) Both $Mg_{60}Zn_{35}Ca_5$ and $Mg_{59}Zn_{35}Ca_5Y_1$ parts exhibited favorable biocompatibility and could be evaluated to be grade 0−1.

Credit authors statement

Cheng Chen: Writing – original draft, Investigation, Methodology, Experiment, Data curation, Writing – review & editing. **Shaoyu Li:** Investigation, Experiment. **Chenrong Ling:** Investigation, Data curation, Writing – review & editing. **Youwen Yang:** Investigation, Data curation, Writing – review & editing. **Chengde Gao:** Supervision, Methodology. **Yageng Li:** Conceptualization, Data curation. **Xinyi Xiao:** Conceptualization, Data curation. **Wenhao Zhou:** Conceptualization, Data curation. **Cijun Shuai:** Resources, Supervision, Conceptualization, Methodology.

Declaration of competing interest

The authors declare that they have no competing financial interests that could have influenced the work reported in this paper.

Acknowledgements

This study was supported by National Natural Science Foundation of China [51935014, 52165043]; JiangXi Provincial Natural Science Foundation of China [20224ACB204013, 20224ACB214008]; Jiangxi Provincial Cultivation Program for Academic and Technical Leaders of Major Subjects [20225BCJ23008]; and Anhui Provincial Natural Science Foundation of China [2308085ME171].

References

[1] Tsakiris V, Tardei C, Clicinschi FM. Biodegradable Mg alloys for orthopedic implants – a review. J Magnes Alloy 2021;9(6):1884–905. https://doi.org/10.1016/j.jma.2021.06.024.

[2] Li Y, Zhou J, Pavanram P, Leeflang MA, Fockaert LI. Pouran,et al. Additively manufactured biodegradable porous magnesium. Acta Biomater 2018;67:378–92. https://doi.org/10.1016/j.actbio.2017.12.008.

[3] Li Y, Jahr H, Zhang XY, Leeflang MA, Li W. Pouran B., et al. Biodegradation-affected fatigue behavior of additively manufactured porous magnesium. Addit Manuf 2019;28:299–311. https://doi.org/10.1016/j.addma.2019.05.013.

[4] Wang X, Liu X, Dai Y, She J, Zhang D, Qi F, et al. A novel Ca-Mg-P/PDA composite coating of Mg alloys to improve corrosion resistance for orthopedic implant materials. Surf Coat Technol 2023;471:129920. https://doi.org/10.1016/j.surfcoat.2023.129920.

[5] Sezer N, Evis Z, Koç M. Additive manufacturing of biodegradable magnesium implants and scaffolds: review of the recent advances and research trends. J Magnes Alloy 2021;9(2):392–415. https://doi.org/10.1016/j.jma.2020.09.014.

[6] Ling C, Li Q, Zhang Z, Yang Y, Zhou W, Chen W, et al. Influence of heat treatment on microstructure, mechanical and corrosion behavior of WE43 alloy fabricated by laser-beam powder bed fusion. Int J Extrem Manuf 2023;6(1):015001. https://doi.org/10.1088/2631-7990/acfad5.

[7] Li K, Liang L, Du P, Cai Z, Xiang T, Kanetaka H, et al. Mechanical properties and corrosion resistance of powder metallurgical Mg-Zn-Ca/Fe bulk metal glass composites for biomedical application. J Mater Sci Technol 2022;103:73–83. https://doi.org/10.1016/j.jmst.2021.07.006.

[8] Liu C, Wang Q, Han B, Luan J, Kai J-J, Liu C-T, et al. Second phase effect on corrosion of nanostructured Mg-Zn-Ca dual-phase metallic glasses. J Magnes Alloy 2021;9(5):1546–55. https://doi.org/10.1016/j.jma.2021.03.016.

[9] Hu T, Yang C, Lin S, Yu Q, Wang G. Biodegradable stents for coronary artery disease treatment: recent advances and future perspectives. Mater Sci Eng C 2018;91:163–78. https://doi.org/10.1016/j.msec.2018.04.100.

[10] Lu W, He M, Yu D, Xie X, Wang H, Wang S, et al. Ductile behavior and excellent corrosion resistance of Mg-Zn-Yb-Ag metallic glasses. Mater Des 2021;210:110027. https://doi.org/10.1016/j.matdes.2021.110027.
[11] Yang Y, He C, Dianyu E, Yang W, Qi F, Xie D, et al. Mg bone implant: features, developments and perspectives. Mater Des 2020:185108259. https://doi.org/10.1016/j.matdes.2019.108259.
[12] Nasr Azadani M, Zahedi A, Bowoto OK, Oladapo BI. A review of current challenges and prospects of magnesium and its alloy for bone implant applications. Prog Biomater 2022;11(1):1–26. https://doi.org/10.1007/s40204-022-00182-x.
[13] Tsai M-H, Yang C-M, Chen Y-H, Chen I-G, Lin C-F, Tseng C-C. Hot pressing of DCPD-coated Mg-Zn-Ca powder: corrosion behavior observed using liquid cell transmission electron microscopy. Mater Des 2023;226:111643. https://doi.org/10.1016/j.matdes.2023.111643.
[14] Wang J, Meng L, Xie W, Ji C, Wang R, Zhang P, et al. Corrosion and in vitro cytocompatibility investigation on the designed Mg-Zn-Ag metallic glasses for biomedical application. J Magnes Alloy 2022. https://doi.org/10.1016/j.jma.2022.09.025.
[15] Wang C, Shuai Y, Yang Y, Zeng D, Liang X, Peng S, et al. Amorphous magnesium alloy with high corrosion resistance fabricated by laser powder bed fusion. J Alloys Compd 2022;897:163247. https://doi.org/10.1016/j.jallcom.2021.163247.
[16] Gu X, Zheng Y, Zhong S, Xi T, Wang J, Wang W. Corrosion of, and cellular responses to Mg–Zn–Ca bulk metallic glasses. Biomaterials 2010;31(6):1093–103. https://doi.org/10.1016/j.biomaterials.2009.11.015.
[17] Lee JI, Ryu WH, Yoon KN, Park ES. In-situ synthesis of Mg-based bulk metallic glass matrix composites with primary α-Mg phases. J Alloys Compd 2021;879:160417. https://doi.org/10.1016/j.jallcom.2021.160417.
[18] Wu G, Chan K-C, Zhu L, Sun L, Lu J. Dual-phase nanostructuring as a route to high-strength magnesium alloys. Nature 2017;545(7652):80–3. https://doi.org/10.1038/nature21691.
[19] Inoue A, Kong FL, Zhu SL, Shalaan E, Al-Marzouki FM. Production methods and properties of engineering glassy alloys and composites. Intermetallics 2015;58:20–30. https://doi.org/10.1016/j.intermet.2014.11.001.
[20] Wu W, Li X, Liu Q, Hsi Fuh JY, Zheng A, Zhou Y, et al. Additive manufacturing of bulk metallic glass: principles, materials and prospects. Mater Today Adv 2022;16:100319. https://doi.org/10.1016/j.mtadv.2022.100319.
[21] Shen Y, Li Y, Chen C, Tsai H-L. 3D printing of large, complex metallic glass structures. Mater Des 2017;117:213–22. https://doi.org/10.1016/j.matdes.2016.12.087.
[22] Zhang C, Ouyang D, Pauly S, Liu L. 3D printing of bulk metallic glasses. Mater Sci Eng R Rep 2021;145:100625. https://doi.org/10.1016/j.mser.2021.100625.
[23] Liu L, Wang D, Deng G, Liu Z, Tan C, Zhou X, et al. Crack inhibition to enhance strength-ductility of CM247LC alloy fabricated by laser powder bed fusion. Mater Sci Eng A 2023;875:145114. https://doi.org/10.1016/j.msea.2023.145114.
[24] Xiao Y, Yang Y, Wang D, Liu L, Liu Z, Wu S, et al. In-situ synthesis of high strength and toughness TiN/Ti6Al4V sandwich composites by laser powder bed fusion under a nitrogen-containing atmosphere. Compos B Eng 2023;253:110534. https://doi.org/10.1016/j.compositesb.2023.110534.
[25] Zhao D, Han C, Peng B, Cheng T, Fan J, Yang L, et al. Corrosion fatigue behavior and anti-fatigue mechanisms of an additively manufactured biodegradable zinc-magnesium gyroid scaffold. Acta Biomater 2022;153:614–29. https://doi.org/10.1016/j.actbio.2022.09.047.
[26] Shi Y. Additive manufacturing of metallic components. Chin J Mech Eng: Addit Manuf Front 2022;1(3):100047. https://doi.org/10.1016/j.cjmeam.2022.100047.
[27] Li D, Xiong Z. Bio-3D printing. Chin J Mech Eng: Addit Manuf Front 2022;1(2):100027. https://doi.org/10.1016/j.cjmeam.2022.100027.
[28] Gao C, Yao X, Deng Y, Pan H, Shuai C. Laser-beam powder bed fusion followed by annealing with stress: a promising route for magnetostrictive improvement of polycrystalline Fe81Ga19 alloys. Addit Manuf 2023;68:103516. https://doi.org/10.1016/j.addma.2023.103516.
[29] Mahbooba Z, Thorsson L, Unosson M, Skoglund P, West H, Horn T, et al. Additive manufacturing of an iron-based bulk metallic glass larger than the critical casting thickness. Appl Mater Today 2018;11:264–9. https://doi.org/10.1016/j.apmt.2018.02.011.
[30] Zhang C, Li X-m, Liu S-Q, Liu H, Yu L-J, Liu L. 3D printing of Zr-based bulk metallic glasses and components for potential biomedical applications. J Alloys Compd 2019;790:963–73. https://doi.org/10.1016/j.jallcom.2019.03.275.
[31] Li K, Li B, Du P, Xiang T, Yang X, Xie G. Effect of powder size on strength and corrosion behavior of Mg66Zn30Ca4 bulk metallic glass. J Alloys Compd 2022;897:163219. https://doi.org/10.1016/j.jallcom.2021.163219.
[32] Gao C, Li C, Peng S, Shuai C. Spiral-eutectic-reinforced biodegradable Zn–Mg–Ag alloy prepared via selective laser melting. Chin J Mech Eng: Addit Manuf Front 2022;1(2):100022. https://doi.org/10.1016/j.cjmeam.2022.100022.
[33] Shi Y, Xue Z, Li P, Yang S, Zhang D, Zhou S, et al. Surface modification on biodegradable zinc alloys. J Mater Res Technol 2023;25:3670–87. https://doi.org/10.1016/j.jmrt.2023.06.149.
[34] Zhao Y-Y, Men H, Estévez D, Liu Y, Wang X, Li R-W, et al. Mg-based bulk metallic glass composite containing in situ microsized quasicrystalline particles. Scr Mater 2014;78–79:21–4. https://doi.org/10.1016/j.scriptamat.2014.01.019.
[35] Chen X, Ning S, Wang A, Le Q, Liao Q. Jia Y.,et al. Microstructure, mechanical properties and corrosion behavior of quasicrystal-reinforced Mg-Zn-Y alloy subjected to dual-frequency ultrasonic field. Corros Sci 2020;163:108289. https://doi.org/10.1016/j.corsci.2019.108289.
[36] Tahreen N, Chen DL. A critical review of Mg–Zn–Y series alloys containing I, W, and LPSO phases. Adv Eng Mater 2016;18(12):1983–2002. https://doi.org/10.1002/adem.201600393.
[37] Lu Y, Bradshaw AR, Chiu YL, Jones IP. Effects of secondary phase and grain size on the corrosion of biodegradable Mg–Zn–Ca alloys. Mater Sci Eng C 2015;48:480–6. https://doi.org/10.1016/j.msec.2014.12.049.
[38] Zhang C, Wu L, Liu H, Huang G, Jiang B, Atrens A, et al. Microstructure and corrosion behavior of Mg-Sc binary alloys in 3.5 wt.% NaCl solution. Corros Sci 2020;174:108831. https://doi.org/10.1016/j.corsci.2020.108831.
[39] Fu XL, Tan MJ, Chen Y, Jarfors AEW, Gupta M, Shek CH. High temperature deformation behavior of Mg67Zn28Ca5 metallic glass and its composites. Mater Sci Eng A 2015;621:1–7. https://doi.org/10.1016/j.msea.2014.10.051.
[40] Matias TB, Roche V, Nogueira RP, Asato GH, Kiminami CS, Bolfarini C, et al. Mg-Zn-Ca amorphous alloys for application as temporary implant: effect of Zn content on the mechanical and corrosion properties. Mater Des 2016;110:188–95. https://doi.org/10.1016/j.matdes.2016.07.148.
[41] Wang J, Li Y, Huang S, Wei Y, Xi X, Cai K, et al. Effects of Y on the microstructure, mechanical and bio-corrosion properties of Mg–Zn–Ca bulk metallic glass. J Mater Sci Technol 2014;30(12):1255–61. https://doi.org/10.1016/j.jmst.2014.11.007.
[42] Yu Z, Liu L, Mansoor A, Liu K, Li S, Du W. Microstructures and mechanical properties of as-extruded Mg–8Gd–2Y–1Zn–6Li alloy. J Alloys Compd 2021;864:158826. https://doi.org/10.1016/j.jallcom.2021.158826.
[43] Huang H, Tian Y, Yuan G, Chen C, Wang Z, Ding W, et al. Dislocations in icosahedral quasicrystalline phase embedded in hot-deformed Mg alloys. J Alloys Compd 2016;658:483–7. https://doi.org/10.1016/j.jallcom.2015.10.284.
[44] Huang H, Kato H, Chen C, Wang Z, Yuan G. The effect of nanoquasicrystals on mechanical properties of as-extruded Mg–Zn–Gd alloy. Mater Lett 2012;79:281–3. https://doi.org/10.1016/j.matlet.2012.04.018.
[45] Zhao C, Shi B, Chen S, Du D, Sun T, Simonds BJ, et al. Laser melting modes in metal powder bed fusion additive manufacturing. Rev Mod Phys 2022;94(4):045002. https://doi.org/10.1103/RevModPhys.94.045002.
[46] Gao X, Lin X, Yu J, Li Y, Hu Y, Fan W, et al. Selective Laser Melting (SLM) of in-situ beta phase reinforced Ti/Zr-based bulk metallic glass matrix composite. Scr Mater 2019;171:21–5. https://doi.org/10.1016/j.scriptamat.2019.06.007.
[47] Liu H, Jiang Q, Huo J, Zhang Y, Yang W, Li X. Crystallization in additive manufacturing of metallic glasses: a review. Addit Manuf 2020;36:101568. https://doi.org/10.1016/j.addma.2020.101568.
[48] Guo FQ, Poon SJ, Shiflet GJ. Enhanced bulk metallic glass formability by combining chemical compatibility and atomic size effects. J Appl Phys 2004;97(1):013512. https://doi.org/10.1063/1.1839221.
[49] Bai Y, Ye B, Guo J, Wang L, Kong X, Ding W. Mechanical properties and yield asymmetry of Mg-Y-Zn alloys: competitive behavior of second phases. Mater Charact 2020;164:110301. https://doi.org/10.1016/j.matchar.2020.110301.
[50] Kiani F, Wen C, Li Y. Prospects and strategies for magnesium alloys as biodegradable implants from crystalline to bulk metallic glasses and composites—a review. Acta Biomater 2020;103:1–23. https://doi.org/10.1016/j.actbio.2019.12.023.
[51] Liang S-X, Jia Z, Liu Y-J, Zhang W, Wang W, Lu J, et al. Compelling rejuvenated catalytic performance in metallic glasses. Adv Mater 2018;30(45):1802764. https://doi.org/10.1002/adma.201802764.
[52] De Giacomo A, Dell'Aglio M, De Pascale O. Single pulse-laser induced breakdown spectroscopy in aqueous solution. Appl Phys A 2004;79(4):1035–8. https://doi.org/10.1007/s00339-004-2622-1.
[53] Cesarz-Andraczke K, Nowosielski R. Surface structure and corrosion behavior of Mg68−xZn28+xCa4(x = 0.4) bulk metallic glasses after immersion in ringer's solution. J Mater Eng Perform 2019;28(4):2365–77. https://doi.org/10.1007/s11665-019-04001-6.
[54] Chen J, Zhang X, Zou L, Yu Y, Li Q. Effect of precipitate state on the stress corrosion behavior of 7050 aluminum alloy. Mater Charact 2016;114:1–8. https://doi.org/10.1016/j.matchar.2016.01.022.
[55] Yang C-M, Chen Y-H, Tsai M-H, Hsu BB-Y, Tsai W-T, Lin C-F, et al. Observation of morphology and compositional changes of magnesium alloy using liquid cell TEM. J Mater Res Technol 2022;21:4548–57. https://doi.org/10.1016/j.jmrt.2022.11.059.
[56] He Y, Wang R, Yang L, Yang L, Liu H, Wang X, et al. Influence of Sc on the microstructure, degradation behavior, biocompatibility in vitro and mechanical property of Mg-2Zn-0.2Zr alloy. Mater Des 2022;221:110863. https://doi.org/10.1016/j.matdes.2022.110863.
[57] Wen Y, Liu Q, Wang J, Yang Q, Zhao W, Qiao B, et al. Improving in vitro and in vivo corrosion resistance and biocompatibility of Mg–1Zn–1Sn alloys by microalloying with Sr. Bioact Mater 2021;6(12):4654–69. https://doi.org/10.1016/j.bioactmat.2021.04.043.
[58] Abdel-Gawad SA, Shoeib MA. Corrosion studies and microstructure of Mg−Zn−Ca alloys for biomedical applications. Surface Interfac 2019;14:108–16. https://doi.org/10.1016/j.surfin.2018.11.011.
[59] Chen C, Ling C, Shao Y, Yang Y, Wang D, Shuai C. Quasicrystal-strengthened biomedical magnesium alloy fabricated by laser additive manufacturing. J Alloys Compd 2023;947:169555. https://doi.org/10.1016/j.jallcom.2023.169555.
[60] Wang B, Gao W, Pan C, Liu D, Sun X. Effect of the combination of torsional and tensile stress on corrosion behaviors of biodegradable WE43 alloy in simulated body fluid. J Funct Biomater 2023;14(2):71. https://doi.org/10.3390/jfb14020071.
[61] Bornapour M, Muja N, Shum-Tim D, Cerruti M, Pekguleryuz M. Biocompatibility and biodegradability of Mg–Sr alloys: the formation of Sr-substituted hydroxyapatite. Acta Biomater 2013;9(2):5319–30. https://doi.org/10.1016/j.actbio.2012.07.045.
[62] Mena-Morcillo E, Veleva L. Degradation of AZ31 and AZ91 magnesium alloys in different physiological media: effect of surface layer stability on electrochemical

behaviour. J Magnes Alloy 2020;8(3):667–75. https://doi.org/10.1016/j.jma.2020.02.014.
[63] Jia Y, Duan W, Ba Z, Yin K, Sun T, Wang Y. Simultaneous improvement in surface mechanical properties and corrosion resistance of biomedical ZK60 alloy by Zr and C co-implantation. Vacuum 2023;208:111642. https://doi.org/10.1016/j.vacuum.2022.111642.
[64] Yang Y, Lu C, Shen L, Zhao Z, Peng S, Shuai C. In-situ deposition of apatite layer to protect Mg-based composite fabricated via laser additive manufacturing. J Magnes Alloy 2023;11(2):629–40. https://doi.org/10.1016/j.jma.2021.04.009.
[65] Mao L, shen L, Chen J, Zhang X, Kwak M, Wu Y, et al. A promising biodegradable magnesium alloy suitable for clinical vascular stent application. Sci Rep 2017;7(1):46343. https://doi.org/10.1038/srep46343.